Study of solute segregation behavior at carbide–ferrite interfaces in 16MND5 welds

Leifeng Zhang, Bertrand Radiguet, Patrick Todeschini, Christophe Domain, Yang Shen, Philippe Pareige

Study of solute segregation behavior at carbide-ferrite interfaces in 16MND5 welds

Leifeng Zhang[a]*, Bertrand Radiguet[a]*, Patrick Todeschini[b], Christophe Domain[b], Yang Shen[c], Philippe Pareige[a]

[a] *Groupe de Physique des Matériaux, UMR CNRS 6634, Université de Rouen Normandie et INSA de Rouen, 76800 Rouen, France*

[b] *Département Matériaux et Mécanique des Composants, EDF R&D, Site des Renardières-Ecuelles, 77818 Moret-sur-Loing cedex, France*

[c.] *LIDEC, Direction Industrielle, EDF DIPNN, 37420 Avoine cedex, France*

**E-mail : wwwxyxy@163.com;*

bertrand.radiguet@univ-rouen.fr.

Abstract

The solute segregation behavior at two types of carbide-ferrite interfaces was investigated by Atom Probe Tomography (APT) technique in a 16MND5 weld before and after ion irradiation. The two types of carbides are cementite and $M_{2.0\text{-}3.2}C$ carbides. Effects of these intergranular carbides on solute segregation behavior at the vicinal Grain Boundaries (GBs) were discussed. No influence was observed within the first tens of nm away from carbides. However, these carbides introduce effective sites for solute segregation (P, Mn, Si and Ni). The segregation of one or several chemical species was observed at interfaces. It is also revealed that the intersection region between carbide and the adjacent GB favors higher P segregation than any other region. After ion irradiation, there is a significant increase of P segregation level at both cementite-ferrite interfaces and $M_{2.0\text{-}3.2}C$ carbide-ferrite interfaces, which could be attributed to a Radiation Enhanced Segregation (RES) of P. The increased P

segregation at interfaces could contribute to the radiation embrittlement. Under both conditions, there is a higher average P segregation level at cementite-ferrite interfaces than $M_{2.0\text{-}3.2}C$ carbide-ferrite interfaces.

Key words: Interfaces; APT; segregation; carbide; ion irradiation; RES mechanism

Highlights

• A higher P segregation level at cementite-ferrite interfaces than $M_{2.0\text{-}3.2}C$ carbide-ferrite interfaces

• No influence of the intergranular carbides on solute segregation behavior at the vicinal GBs (within the first tens of nm from carbides)

• A higher P segregation at the intersection region between carbide and GB

• The RES mechanism of P at carbide-ferrite interfaces after ion irradiation

1. Introduction

Reactor Pressure Vessel (RPV) steels may embrittle gradually during operation. This embrittlement is mainly attributed to a hardening mechanism, related to the formation of Cu-rich [1, 2] and Ni, Mn, Si-rich features [3-5]. Besides, a non-hardening mechanism, resulting from intergranular P segregation that impairs the GB cohesion, could also contribute to irradiation embrittlement [6, 7]. APT analyses on Russian VVER-1000 RPV base and welds revealed a significant GB segregation of P (and other alloying elements) [8]. It was also reported that the non-hardening mechanism could contribute to the total radiation embrittlement of VVER-1000 RPV welds throughout its extended lifetime [9]. P segregation phenomenon could be of critical importance during long-term safe service of RPV steels.

Interfaces between second-phase particles and the matrix, acting as energetically favorable sites, could also provide preferential sites for P segregation. The carbide-ferrite interfacial segregation of P was reported in RPV steels [10, 11] and other steels [12-16]. Previous Auger Electron Spectroscopy (AES) results revealed that, on the fracture surface of Russian VVER-1000 steels, lots of large-sized $M_{23}C_6$ carbides were observed at GBs, and that the acquired P peak seems even higher at these $M_{23}C_6$ carbide-ferrite interfaces than at the GBs without carbide decoration [11]. Besides P, other impurities like S [16] and H [17] could also be trapped at carbide-ferrite interfaces. Whether there is a strong P segregation at carbide-ferrite interfaces and how it evolves under irradiation appear to be important. Besides, solute transportation occurs during the formation and growth of GB carbides. Whether there is an influence of these intergranular carbides on solute segregation behavior at adjacent GBs remains unclear. All these issues are quite interesting in material science field, and thus extensive investigation of GB carbide chemistry and carbide-ferrite interfacial segregation behavior should be performed.

APT is a robust technique in quantifying local 3D chemical composition at the atomic scale [18]. Furthermore the crystallographic details, as provided by electron microscopies, can be correlated to APT data [19]. In recent years, the correlative Transmission Electron Microscopy (TEM)/APT approach [20, 21], or the correlative Electron Backscattering Diffraction (EBSD)/Transmission Kikuchi Diffraction (TKD)/APT methodology [22-28], has been applied to bridge the relationship between microchemistry and GB character. AES technique, when combined with EBSD, can also achieve both the crystallographic details and chemical information, but the chemical information is confined to 2 dimensions. Compared with AES technique focusing on brittle systems, the Focused Ion Beam (FIB) sample preparation routine renders the interface solute segregation analyses feasible in non-brittle systems with APT.

In the present work, the solute segregation behavior at carbide-ferrite interfaces was quantitatively studied in both a non-irradiated (reference) weld and an ion-irradiated weld by the correlative EBSD/TKD/APT methodology [24, 28, 29]. The chemical compositions of these carbides (2 types) and the influence of these carbides on solute segregation behavior at adjacent GBs were also investigated in this article.

2. Experimental method

2.1 Materials, sample preparation and experimental conditions

The studied material is a 16MND5 weld fabricated with the submerged arc welding process. Its chemical composition is listed in Table 1. The P content is 80 wt.ppm (or 140 at.ppm). The specimens of the welds originated from the welding center of the circumferential welding seam, which has a size of 4.4 m in diameter. The post welding heat treatment was performed at 595~610°C for 16.5 h, followed by a controlled cooling at 15°C/h down to 350°C and then air cooling to ambient temperature.

Table 1 Bulk chemical composition of the 16MND5 weld steel

	C	P	Si	Mn	Ni	Cr	Mo	Cu	Fe
wt.%	0.07	0.008	0.43	1.57	0.75	0.16	0.58	0.04	Bal.
at.%	0.34	0.014	0.84	1.60	0.72	0.18	0.34	0.035	Bal.

The ion irradiation experiments were performed at 400°C in JANNUS facility in Orsay, France. As shown in Fig. 1a, two thin foils, with a diameter of 3 mm, were cut from the reference weld for irradiation experiments. The detailed information about ion irradiation is given in Table 2. According to the calculation from SRIM software using the modified Kinchin-Pease model with a displacement threshold energy of 40 eV [30], the received dose is about 0.1 dpa at a depth from 300 and 600nm. There is nearly no influence of implanted ions at this irradiation depth. The dose amount, 0.1 dpa, is similar to a 40 years' operation condition of some Pressurized Water Reactors (PWRs) [31].

Table 2 5 MeV Fe^{3+} ion irradiation conditions. Dose and dose rate are obtained from SRIM calculations at an irradiation depth of 300 to 600 nm, where the samples were prepared in this region.

Fluence ($\times10^{14}$ at/cm^2)	Dose (dpa)	Flux ($\times10^{10}$ ions/cm^2/s)	Dose rate ($\times10^{-5}$ dpa/s)	Irradiation time (min)	T (°C)
2.85	~0.1	3.96	1.3	120	400±5

First, the microstructure was observed by Scanning Electron Microscopy (SEM) and EBSD in dual-beam SEM/FIB instruments (Zeiss Nvision 40 with the AZtec acquisition software and Zeiss XB 540 with the TEAM-EDAX software). Specimens for SEM/EBSD analyses, in the shape of thin slices of 10×10×0.3 mm^3, were cut from as-received half Charpy sample (after Charpy impact tests) and then fixed into a conductive resin with a diameter of 25 mm. Afterwards, the specimens were grinded with coarse, medium and fine sandpaper discs and then polished on special cloths with various diamond liquids. The samples were finally

polished in a semi-automatic polishing machine for 30 min using a 0.04 μm colloidal silica suspension (Struers OP-S). Samples for SEM observations were finally chemically etched with 1% Nital solution for 60 s. The EBSD experiments were performed at 20 kV at a working distance of 10 mm.

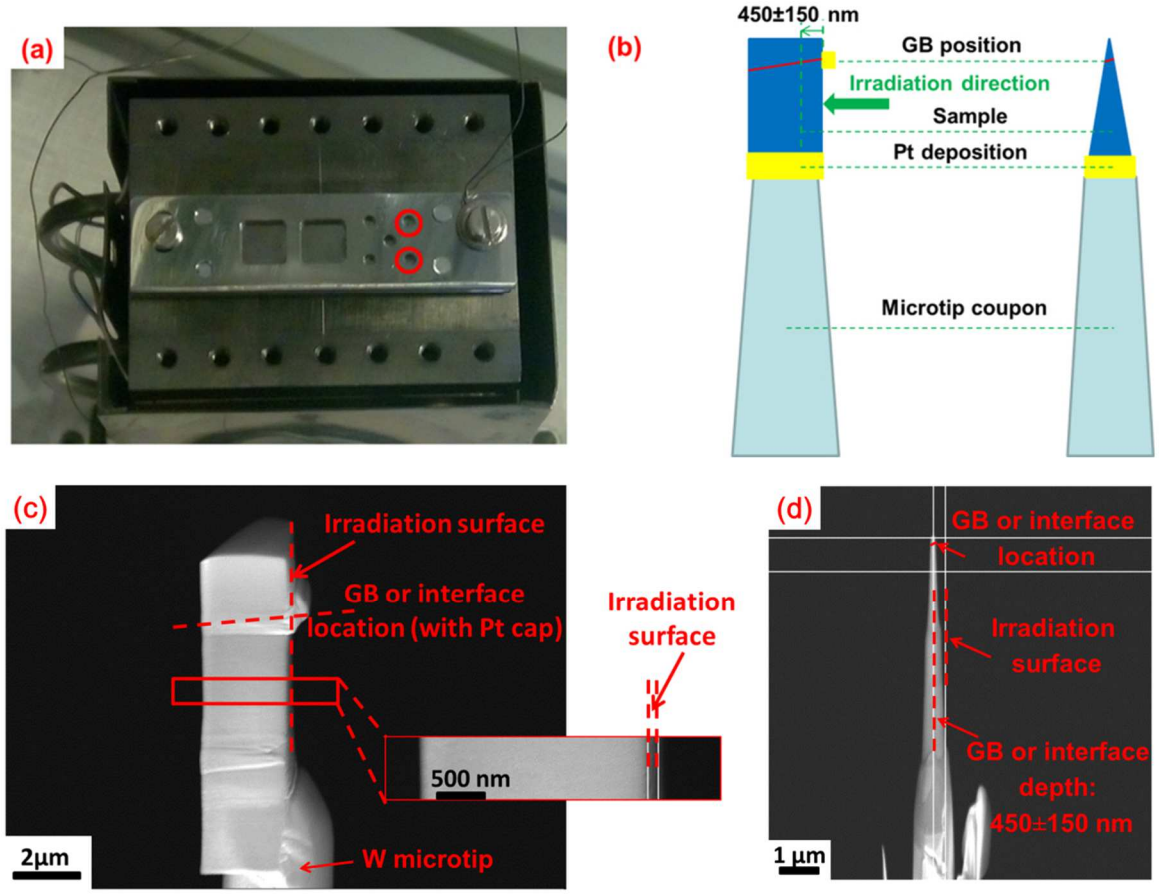

Fig. 1 Illustrations of ion-irradiated sample preparation procedures for APT experiments: (a) two thin foils (3 mm in diameter) in the sample holder for ion irradiation experiments; (b) the schematic APT sample preparation routes with a specific GB (or interface) being located at the apex (less than 100 nm) of the thin tip after annular milling; (c) the positioning of the lift-out chunk (in SEM view) containing a specific GB or interface on a W microtip for the subsequent annular milling; (d) the final tip with the GB or interface being placed within the first 100 nm from the apex. The two thin foils cut from the reference weld are marked with red circles in (a) and the GBs are shown in solid red lines in (b). In (c) & (d), the image contrast was observed by the in-lens detector. And the irradiation surface planes are particularly located in order to be nearly perpendicular to the present

SEM view planes, with a deviation of less than 100 nm (in the local magnification figure of (c)). In this case, after careful manipulations during TKD-aided annular milling, all the identified GBs or interfaces were finally extracted from a certain irradiation depth (450±150 nm) beneath the irradiation surface.

The detailed APT sample preparation route for the reference weld can be referred to the literature [28, 29]. After characterizing the microstructure and picking up a specific feature (GB or carbide-ferrite interface), FIB was utilized to mill a wedge-shaped chunk. Then, a micromanipulator and a Gas Injection System (GIS) were used to lift out the chunk containing the specific GB or interface, which was subsequently placed on the cap of a W microtip. During the subsequent annular milling, FIB was used as a milling tool to sharpen the tip at 30 kV, with the beam currents decreasing successively from 700 pA to 40-50 pA. To minimize the Ga^+ contamination layer in the tip, the final cleaning procedure was performed at 2 kV with a current of 100 pA. TKD was used during the final steps of annular milling to identify the GB position. In the final tip, a GB or an interface was located in the first 100 nm from the apex.

Since irradiation damage depends on the depth, it is important to have an accurate estimation of the initial depth of the GB finally located close to the tip apex. As schematically illustrated in Fig. 1b, the lift-out chunk containing the specific feature was extracted and mounted to a microtip. In practice, it was positioned in a manner that the irradiated surface is nearly perpendicular to the SEM view plane. As exhibited in Fig. 1c & d, the spacing between the final tip apex and the irradiated surface plane can be controlled at each step. It is equal to (450±150 nm). The location of the GB or interface appearing in the needle is controlled with TKD imaging between the final steps of annular milling. These procedures ensure that the analyzed feature from a depth of 300-600 nm beneath the irradiated surface is finally located in the first 100 nm of the needle.

Microanalyses were carried out with a Local Electrode Atom Probe (LEAP 4000 XHR, CAMECA) operated at a temperature of 55 K, a detection rate of 0.15%, a pulse repetition rate of 200 kHz and a pulse fraction equal to 20% of the standing voltage. For the 3D data reconstruction, both the commercial IVAS software (CAMECA, v. 3.6.6) and the GPM 3D software (from GPM lab, v. 6.3) were used.

2.2 Data analyses for GB chemistry, carbide chemistry and crystallography

2.2.1 Calculation of the GB or carbide-ferrite interfacial excess

During the evaporation of carbide, there is always an enhanced formation of molecular ions and multiple events [31]. For carbides, the C peaks $^{12}C^{2+}$, $^{13}C^{2+}$, $^{12}C^{+}$, $^{24}(C_2)^{2+}$, $^{13}C^{+}$, $^{36}(C_3)^{2+}$, $^{37}(C_3)^{2+}$, $^{24}(C_2)^{+}$, $^{48}(C_4)^{2+}$, $^{49}(C_4)^{2+}$, $^{36}(C_3)^{+}$, $^{37}(C_3)^{+}$, $^{48}(C_4)^{+}$ were considered. Fig. 2 shows examples of mass spectra in the range 22~30 amu., for both Mo-enriched carbides (Fig. 2a) and ferrite phase (Fig. 2b). For the possible peak overlapping in the cases like $^{54}Cr^{2+}/^{54}Fe^{2+}$, $^{58}Ni^{2+}/^{58}Fe^{2+}$, $^{64}Ni^{2+}/^{96}Mo^{3+}$, $^{12}C^{+}/^{24}(C_2)^{2+}$, $^{36}(C_3)^{2+}/^{54}Fe^{3+}$, $^{24}(C_2)^{+}/^{48}(C_4)^{2+}/^{96}Mo^{4+}$ (in case of Mo-enriched carbides), $^{49}(C_4)^{2+}/^{98}Mo^{4+}$, $^{50}Cr^{2+}/^{100}Mo^{4+}$, $^{48}(C_4)^{+}/^{96}Mo^{2+}$, the peak decomposition was calculated based on the natural isotope abundances [18].

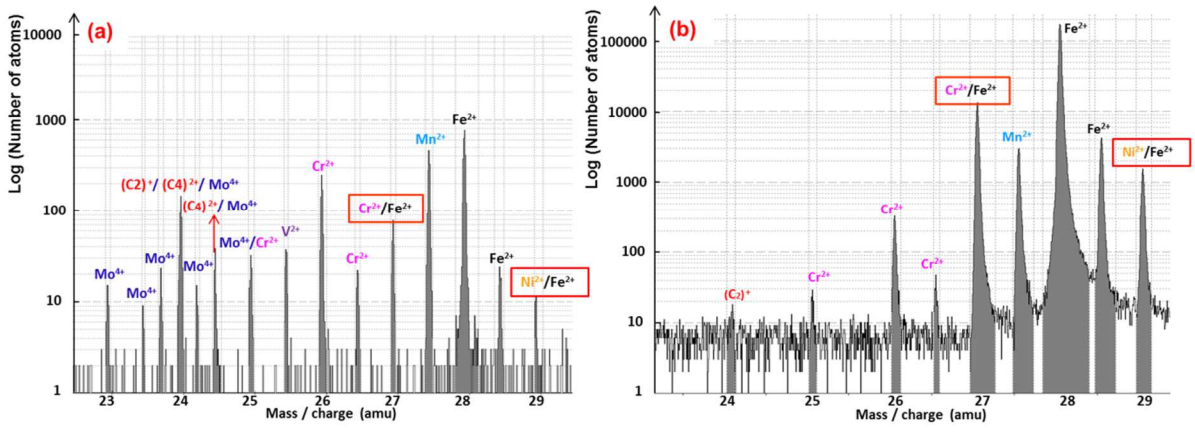

Fig. 2 Partial mass spectra exhibiting the region between 22 and 30 amu. from APT analyses for (a) a Mo-enriched carbide and (b) the ferrite matrix [28]. Peaks are identified and peak overlaps are shown.

The concentration of an element is calculated from the proportion of detected ions after identifying each isotope and removing the corresponding background noise. If considering only the statistical variation, the standard deviation on the measured concentration of element i, σ_i, is given by:

$$\sigma_i = \sqrt{\frac{X_i(1-X_i)}{N_{at}}}$$

where X_i is the measured concentration of solute i and N_{at} is the total number of atoms in the analyzed volume.

For calculation of GB or interfacial segregation, a general method based on the Gibbsian interfacial excess Γ_i [32] was adopted. The Γ_i value (in atoms/nm^2) is defined as:

$$\Gamma_i = \frac{N_i^{\text{excess}}}{\eta \cdot A}$$

where N_i^{excess} is the number of atoms in excess determined from cumulative profile, η is the detection efficiency of the LEAP and A is the interfacial area on which the measurement is done. The illustration of Γ_i can be referred to our previous work [28, 29] and η equals to 0.36 for LEAP 4000 XHR. In the above equation, the error bar of Γ_i, $\sigma_{\Gamma i}$, can be calculated by substituting N_i^{excess} with its uncertainty, $\Delta N_i^{\text{excess}}$, from the cumulative profile. Here, for solute element i, N_i^{excess} and $\Delta N_i^{\text{excess}}$ correspond to X_i and σ_i, respectively.

2.2.2 Identification of crystallographic detail

During APT analyses, GB carbides were intercepted (as shown later). For a specific GB, 5

Degrees of Freedom (DOFs, or five independent parameters) are needed to fully describe its structure. Three DOFs of a GB between grain A and B, including one for misorientation angle θ and two for rotation axis $\boldsymbol{c} = [h_o\, k_o\, l_o]$ are used to define the mutual misorientation between the two crystals, and two DOFs are applied to depict the GB planes $(h_{nA}\, k_{nA}\, l_{nA})/(h_{nB}\, k_{nB}\, l_{nB})$. Thus, a complete geometry of a GB can be described by: $\theta°[h_o\, k_o\, l_o](h_{nA}\, k_{nA}\, l_{nA})/(h_{nB}\, k_{nB}\, l_{nB})$.

After getting the TKD image during annular milling, the $\theta/\boldsymbol{c}$ pair can be obtained from the software. To recognize the GB plane, both the TKD information and the 3D data reconstruction information need to be combined. This methodology has been reported in our previous papers [28, 29].

3. Results

3.1 Microstructure characterization

The mesoscale microstructure of the reference weld is exhibited in Fig. 3a. Numerous acicular ferrite grains with distinct orientations were observed. These thin grains are arranged in an irregular way, i.e., they intersect with each other. Compared with the "sheaf-like" bainitic ferrite, the acicular ferrite has a "basket-weave" morphology [33]. Numerous carbides are present along the GBs, as shown in Fig. 3b. These carbides have a small size (in nanometer scale) with various shapes: spherical, ellipsoidal, rod-like and plate-like. Thus, the investigated weld mainly has a complex microstructure of acicular ferrite and intergranular carbides. Similar to that reported in the literature [33], the schematic microstructure is illustrated in Fig. 3c. The boundaries are classified as GBs and carbide-ferrite interfaces. After ion irradiation, there is no obvious evolution for the mesoscale microstructure in comparation to the reference weld.

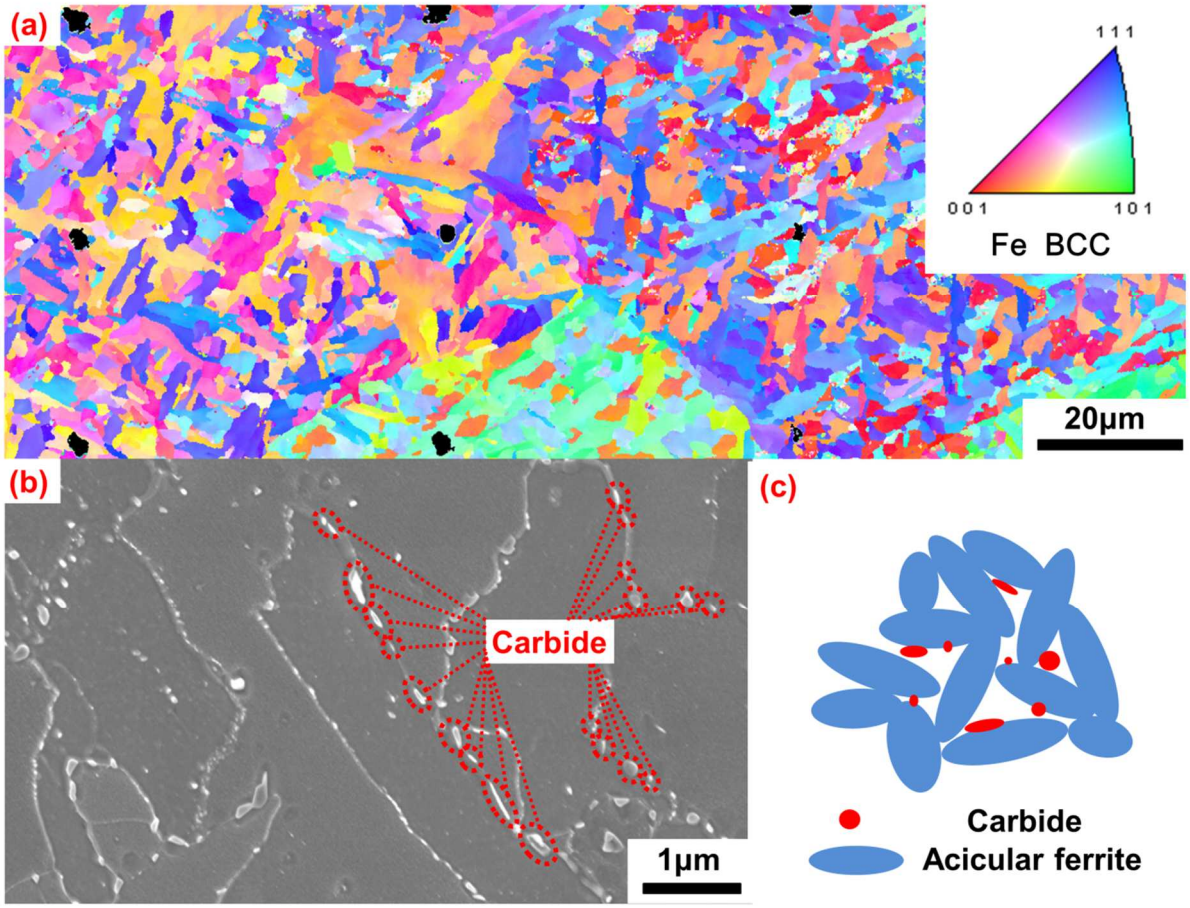

Fig. 3 Characterization of the mesoscale microstructure in the reference weld [28]: (a) inverse pole figure map; (b) SEM image showing the intergranular carbides; (c) schematic illustration of acicular ferrite and carbides (highlighted by red dashed lines). In (a), the 12 black marks were created regularly by FIB milling as complementary signals to identify the relative location of different grains.

3.2 Intergranular carbides

Two types of carbides were detected by APT experiments for both reference and ion-irradiated welds, and no significant evolution of carbides was observed after ion irradiation. First, Mo-rich carbides were observed. Examples of such carbides are shown in Fig. 4a & b. In general, these carbides have a small size (typically smaller than $40\times40\times20$ nm^3) and various shapes (spherical, ellipsoidal, rod-like or plate-like). After chemical composition measurement shown in Table 3 (for the reference weld) and Table 4 (for the ion-irradiated weld), they were identified as $M_{2.0\text{-}3.2}C$ carbides, where M is Fe, Mo, Cr and Mn [34]. The Fe

content is less than 30 at.% while Mo is over 35 at.%. Compared to Mn and Fe, Mo has stronger carbide forming ability [35]. Thus, the $M_{2.0\text{-}3.2}C$ carbide formation is thermodynamically favored compared to Mn-enriched or Fe-enriched carbides. Besides, the low diffusivity of Mo (with an activation energy of 282.6 kJ/mol [36]) as well as its low content in the steel kinetically limits the growth of carbides, resulting in fine precipitation at GBs. From literature, Mo_2C-type carbide was reported in the 16MND5 base metal [34, 37]. However, this is not the same from our experimental results. Besides of the detection deviations due to different atom probe instruments, an influence of thermal history could also be responsible for this gap. Different from the base metal, the weld metal undergoes a complex thermal history, in which various types of carbides could be probably formed.

Besides of being incorporated into the $M_{2.0\text{-}3.2}C$ carbides, Mn also tends to segregate at Mo-enriched carbide-ferrite interfaces as well as the vicinal GBs (Fig. 4a & b). The Mn decoration at carbide-ferrite interfaces, acting as a diffusion barrier, may also suppress the continuous substitution of Fe by Mo into carbides and thus inhibits the further growth of $M_{2.0\text{-}3.2}C$ carbides. This is because the Mn segregation decreases the interfacial energy and pins the interface migration [38]. It seems that the largest $M_{2.0\text{-}3.2}C$ carbides tend to own a plate-like shape. $M_{2.0\text{-}3.2}C$ carbide-ferrite interfaces were selected from these plate-like carbides, as shown in Fig. 4b.

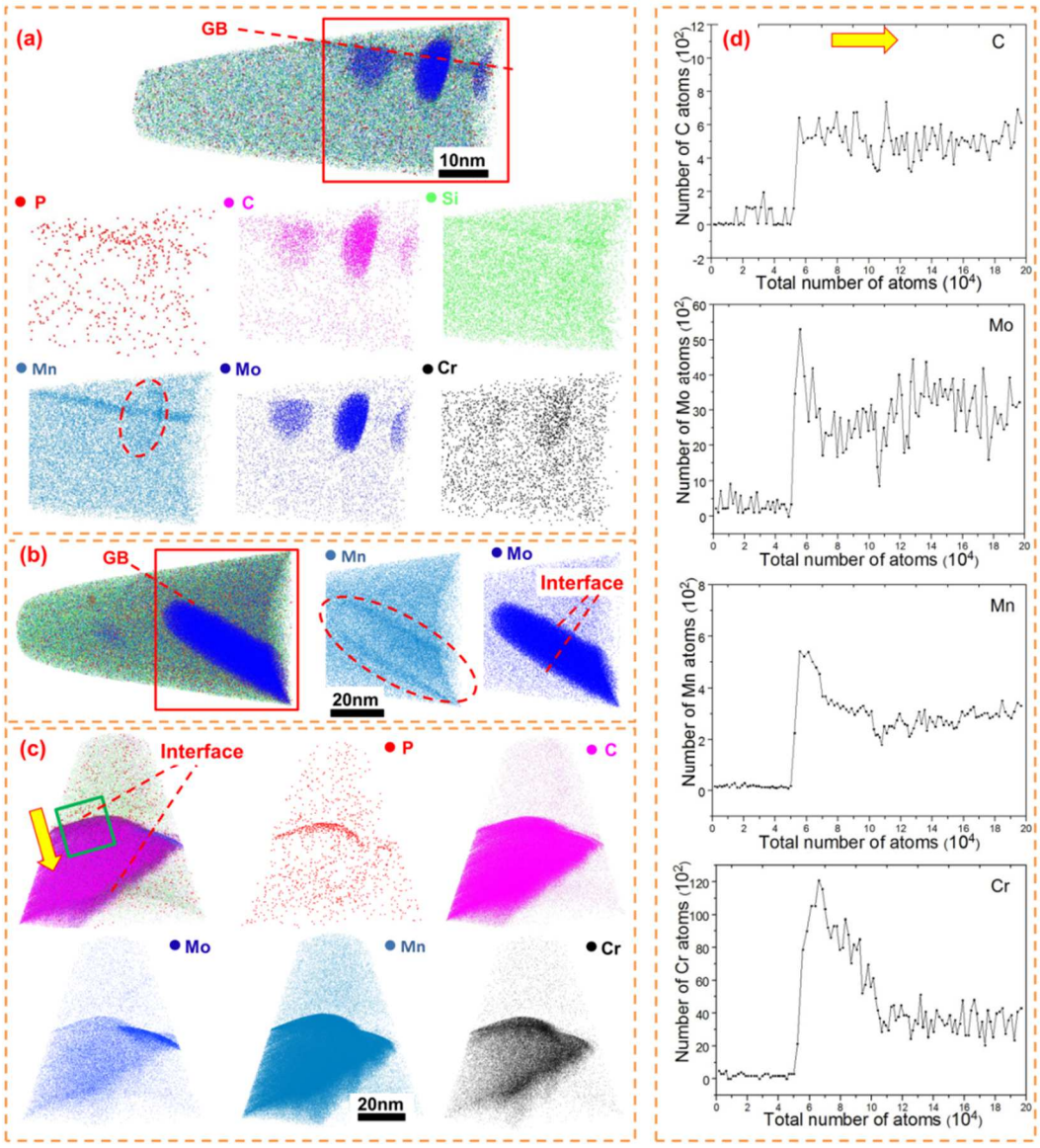

Fig. 4 APT data analyses from the reference weld for (a) a GB decorated with three Mo-enriched carbides ($M_{2.0\text{-}3.2}C$ carbides); (b) a GB decorated with a $M_{2.0\text{-}3.2}C$ carbide and two selected $M_{2.0\text{-}3.2}C$ carbide-ferrite interfaces; (c) a typical Mn, Mo, Cr-enriched carbide (cementite) and two selected cementite-matrix interfaces; (d) concentration profiles (C, Mo, Mn and Cr) through the selected interface in (c) with a horizontal scale of 19.6 nm. In (a), for clarity, P, C, Si, Mn, Mo and Cr maps are also shown, and P, C, Mn and Si segregation at the GB are obvious. In (a) & (b), the Mn segregation at $M_{2.0\text{-}3.2}C$ carbide-ferrite interfaces is obvious, as marked by dashed circle.

The second type of carbides observed here, as exhibited in Fig. 4c, is typically enriched in Fe. It also contains solute elements like Mn, Mo and Cr and possesses a large size (typically

larger than $40\times40\times20$ nm^3). According to the chemical compositions reported in Tables 3 & 4, this second population of carbides has stoichiometry close to M_3C where M consists of Fe, Mn, Mo and Cr (cementite) [34]. According to the results in Table 3 & 4, the Fe concentration is higher than 50 at.%. The outer layers of these carbides are not chemically homogeneous. As exhibited in Fig. 4d, C seems to have a homogeneous distribution while Mn, Mo or Cr presents a heterogeneous one. A clear enrichment of Mo, Mn and Cr elements was observed in the first 2 to 8 nm shell, as reported in similar alloys [39]. The chemical inhomogeneity at cementite-ferrite interface is mainly attributed to the slow diffusion of carbide forming elements (Cr, Mo and Mn) in cementite [39]. The low diffusivity of these elements in cementite seems to act as a kinetic barrier for the accommodation of the incoming atom flux from ferrite [39]. Due to this inhomogeneity of the carbide composition, the Γ_i values of Mn, Mo, Cr and C were not quantified at these interfaces. It can be noticed that the carbide-matrix interfaces are not perfectly flat, similar to the reported $M_{23}C_6$-ferrite interface [14].

According to the measured carbide concentrations from Tables 3 & 4, there exists no difference on the carbide types between the reference and the ion-irradiated welds. And the chemical compositions of the ferrite matrix are also reported for both conditions in Tables 3 & 4. The C, Mo, Cr and Mn contents are lower in ferrite compared to the bulk concentration (Table 1) because these elements are concentrated in carbides. After ion irradiation, there is no significant evolution of carbides. This agrees with the fact that the ferrite composition remains the same level under irradiation.

Table 3 Chemical compositions (in at.%) of the ferrite matrix and the carbides in the reference weld. M/C is the ratio between the concentration of solute elements (Fe, Mn, Mo and Cr) and that of C measured in the detected carbides.

	Cementite				$M_{2.0\text{-}3.2}C$ carbide				
Ferrite	**1**	**2**	**3**	**4**	**A**	**B**	**C**	**D**	**E**

C	0.089±0.002	25.8±0.2	26.0±0.2	24.3±0.2	25.37±0.06	25.5±0.2	27.1±0.4	23.8±0.8	25.0±1.2	29.2±0.5
P	0.016±0.001	-	-	-	-	-	-	-	-	-
Si	0.843±0.005	0.006±0.001	0.02±0.01	0.11±0.01	0.020±0.001	0.20±0.02	0.13±0.04	0.10±0.06	0.3±0.1	0.08±0.03
Cr	0.125±0.002	1.75±0.05	0.61±0.04	0.69±0.03	2.91±0.02	3.21±0.06	1.9±0.1	1.7±0.3	1.6±0.4	1.6±0.2
Mn	1.244±0.006	16.2±0.1	11.5±0.2	5.64±0.08	18.22±0.06	5.25±0.08	3.2±0.2	3.6±0.4	5.6±0.7	4.0±0.2
Ni	0.761±0.005	0.22±0.02	0.33±0.03	0.38±0.02	0.20±0.01	0.19±0.02	0.09±0.03	-	0.2±0.1	0.06±0.03
Cu	0.029±0.001	-	-	-	-	-	-	-	-	-
Mo	0.205±0.003	1.18±0.04	0.47±0.03	0.63±0.03	1.50±0.02	55.3±0.2	60.4±0.5	59.4±1.0	38.0±1.4	55.2±0.6
Fe	Bal.	54.85±0.08	61.09±0.08	68.36±0.06	51.8±0.07	10.55±0.09	7.31±0.08	11.5±0.06	29.6±0.06	9.94±0.08
M/C		2.87	2.83	3.11	2.94	2.91	2.68	3.17	2.93	2.41

Notes: "-" indicates "not detected".

Table 4 Chemical compositions (in at.%) of the ferritic matrix and the carbides in the ion-irradiated weld. M/C is the ratio between the concentration of carbide forming elements (Fe, Mn, Mo and Cr) and that of C.

	Ferrite	**Cementite**					**$M_{2.0\text{-}3.2}C$ carbide**		
		1	**2**	**3**	**4**	**5**	**A**	**B**	**C**
C	0.057±0.001	26.1±0.2	25.80±0.07	24.51±0.07	25.1±0.1	26.34±0.06	30.8±0.2	28.4±0.4	29.3±0.2
P	0.008±0.001	-	-	-	-	-	-	-	-
Si	0.842±0.005	0.02±0	0.02±0	0.06±0	0.05±0.01	0.009±0	0.18±0.02	0.17±0.04	0.24±0.02
Cr	0.128±0.002	2.03±0.05	0.75±0.01	2.29±0.02	4.52±0.06	1.17±0.02	2.24±0.07	2.7±0.2	2.80±0.06
Mn	1.296±0.007	17.0±0.1	9.97±0.05	15.05±0.06	18.0±0.1	8.92±0.04	3.97±0.09	5.0±0.2	4.25±0.08
Ni	0.736±0.005	0.23±0.02	0.31±0.03	0.32±0.01	0.22±0.01	0.26±0.01	0.08±0.01	0.16±0.04	0.10±0.01
Cu	0.033±0.001	-	-	-	-	-	-	-	-
Mo	0.193±0.003	1.03±0.04	0.60±0.01	1.26±0.02	1.24±0.03	1.11±0.01	60.2±0.2	50.1±0.5	59.7±0.2

Fe	Bal.	53.59±0.07	62.55±0.08	56.51±0.08	50.9±0.1	62.19±0.07	2.53±0.07	13.47±0.08	3.61±0.06
M/C	-	2.83	2.88	3.08	2.97	2.80	2.24	2.51	2.41

Notes: "-" indicates "not detected".

3.3 Carbide-ferrite interfacial solute segregation

Table 5 lists the calculated interfacial excess values of identified carbide-ferrite interfaces for various chemical species (P, Si, Mn and Ni) for both unirradiated and ion-irradiated welds. It is inferred that these carbide-ferrite interfaces provide effective sites for the segregation of one or several elements (P, Si, Mn and Ni). Particularly, the segregated Mn content can reach a high value of 5.5±0.2 atoms/nm^2 at $M_{2.0\text{-}3.2}C$ carbide-ferrite interfaces as it can be clearly seen in Fig. 4a & b.

Table 5 Gibbsian interfacial excess values (in atoms/nm^2) of the segregated elements at the interfaces for both the reference and ion-irradiated welds. For each type of interface, the number of investigated features is given into parenthesis.

Element			**P**	**Si**	**Mn**	**Ni**
Reference weld	**Cementite-ferrite interface (9)**	1	0.8±0.4	0.9±0.4	-	0.8±0.1
		2	0.06±0.05	-	-	-
		3	0.2±0.1	-	-	-
		4	0.2±0.1	-	-	-
		5	0.03±0.02	2.8±0.5	-	-
		6	0.4±0.2	-	-	0.3±0.1
		7	0.7±0.2	-	-	-
		8	0.2±0.1	-	-	0.6±0.3
		9	0.8±0.3	-	-	0.6±0.3
	$M_{2.0\text{-}3.2}C$ carbide-ferrite interface (3)	1	0.2±0.1	0.38±0.01	4.0±0.2	-
		2	0.10±0.04	1.7±0.1	5.5±0.2	1.6±0.8
		3	0.14±0.09	0.3±0.1	2.0±0.2	0.6±0.3

Ion-irradiated weld	**Cementite-ferrite interface (14)**	1	0.3±0.2	-	-	-
		2	0.6±0.3	-	-	-
		3	1.0±0.2	-	-	-
		4	0.3±0.1	1.6±0.3	-	-
		5	1.2±0.6	-	-	-
		6	2.9±0.7	-	-	-
		7	1.6±0.6	-	-	-
		8	2.7±0.8	-	-	1.7±1.0
		9	1.5±0.5	1.3±0.3	-	-
		10	2.9±0.9	1.0±0.3	-	1.2±0.7
		11	0.8±0.2	-	-	-
		12	1.6±0.4	-	-	-
		13	1.0±0.2	1.3±0.1	-	1.8±0.9
		14	2.8±1.5	-	-	-
	$M_{2.0\text{-}3.2}C$ carbide-ferrite interface (5)	1	1.6±0.8	0.8±0.2	1.6±0.7	-
		2	0.6±0.5	-	0.7±0.1	-
		3	0.11±0.08	-	0.17±0.01	-
		4	0.2±0.1	-	-	-
		5	1.7±1.5	-	0.6±0.1	-

Notes: "-" means that no significant segregation or depletion is detected.

The peak and average values of P interfacial excess for each type of interface are listed in Table 6. It is clear that the P segregation is more pronounced at the cementite-ferrite interfaces. The variation from one carbide-ferrite interface to another could be attributed to their distinct lattice coherencies with ferrite. Moreover, there is a clear increase of P segregation level for both cementite-ferrite interfaces and $M_{2.0\text{-}3.2}C$ carbide-ferrite interfaces in the ion-irradiated weld. After ion irradiation, there is no clear change except P segregation.

298 **Table 6 Gibbsian interfacial excess values (in atoms/nm^2) of P for the identified interfaces in both welds.**

299 **For each type of interface, the number of investigated features is given into parenthesis.**

	Reference weld		Ion-irradiated weld	
	Cementite-ferrite interfaces (9)	**$Mo_{2.0\text{-}3.2}C$ carbide-ferrite interfaces (3)**	**Cementite-ferrite interfaces (14)**	**$M_{2.0\text{-}3.2}C$ carbide-ferrite interfaces (5)**
Peak	0.8±0.3	0.2±0.1	2.9±0.5	1.7±1.5
Average	0.4±0.2	0.15±0.07	1.4±0.5	0.8±0.6

300 ## 4. Discussion

301 ### 4.1 Influence of intergranular carbides on solute segregation at the adjacent GB

302 GB segregation of P may embrittle the GB cohesion and thus lead to intergranular fracture.
303 An investigation of P segregation behavior at Low Angle Grain Boundaries (LAGBs), general
304 High Angle Grain Boundaries (HAGBs) and Σ3 HAGBs has been reported in our previous
305 research [28]. It is revealed that the average P segregation level is higher in LAGBs or general
306 HAGBs than in Σ3 HAGBs [28].

307 Besides, carbides were observed at GBs. The influence of these carbides on segregation
308 behavior is discussed here. These carbides nucleate and grow along GBs, and some carbide
309 forming elements (C, Mo, Cr and Mn) could gradually diffuse from both their vicinal GBs
310 and the ferrite matrix to the carbides. Consequently, $M_{2.0\text{-}3.2}C$ intergranular carbides may
311 influence solute segregation behavior at adjacent GBs. This influence should be confined to a
312 certain distance away from carbides. Let us examine this point in more details below.

313 As shown in Fig. 5, by plotting concentration profiles through a general HAGB 52°[$\bar{3}3\bar{1}$]($\bar{5}$
314 43)/(65$\bar{5}$) at different distances away from a $M_{2.0\text{-}3.2}C$ carbide, the variations of Gibbsian
315 interfacial excess values with distance from the carbide were quantified and discussed.

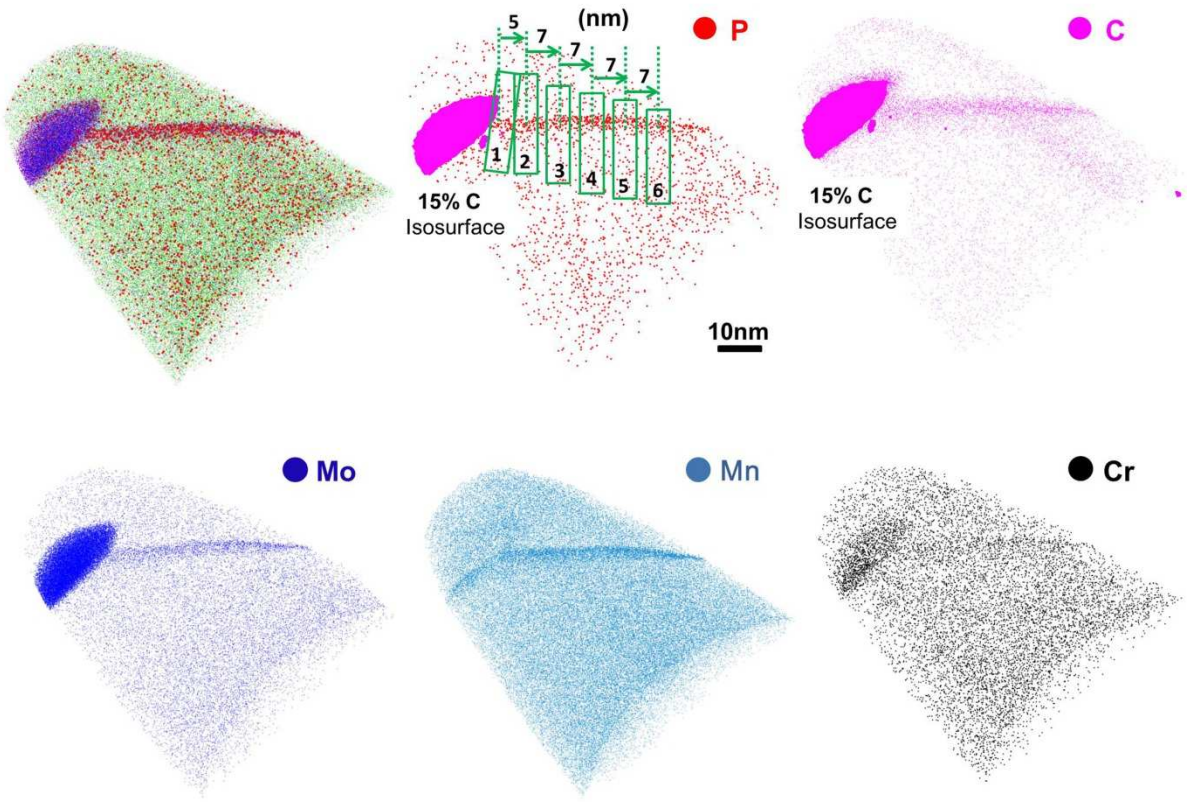

316

317 **Fig. 5 3D reconstruction of a HAGB 52°[$\bar{3}\bar{3}1$]($\bar{5}43$)/($65\bar{5}$) of the reference weld showing the solute**
318 **distribution maps of several chemical species (P, C, Mo, Mn and Cr). Note that, the co-segregation of**
319 **P, C, Mo, Mn and Cr at the HAGB is evident and the 15 at.% C isosurface plots the contour of an**
320 **intergranular $M_{2.0\text{-}3.2}C$ carbide. Six green rectangles (5×35×20 nm^3) illustrate the locations where**
321 **different concentration profiles (spaced at a certain distance along the GB) were plotted. The cuboid**
322 **1 crosses through the intersection region between the GB and the carbide.**

323 The calculated results are reported in Table 7. It is obvious that, within the range of
324 distances investigated (5-36 nm), there is no significant change in the segregation level of
325 carbide forming elements like C, Cr, Mo and Mn. Thus, in the present conditions, these
326 intergranular carbides do not exhibit any obvious influence on the segregation behavior at the
327 adjacent GB. Whether there is a presence of carbides at the GB or not, is not an influencing
328 factor of solute segregation level at the adjacent GB.

329 **Table 7 Gibbsian interfacial excess values (in atoms/nm^2) with different distances from the GB**
330 **position (nm) as given in Fig. 5.**

Position	Distance from carbide (nm)	P	C	Si	Mn	Ni	Cr	Mo
1	**0**	1.6±1.1	n.m.	0.8±0.2	n.m.	0.7±0.5	n.m.	n.m.
2	**5**	0.9±0.6	4.8±2.4	1.8±0.2	8.3±0.8	2.1±0.1	0.3±0.2	2.8±2.0
3	**12**	0.6±0.5	5.1±2.7	-	5.7±0.6	-	0.2±0.1	2.8±2.2
4	**19**	0.8±0.5	5.6±3.1	1.4±0.2	5.9±0.6	-	0.6±0.3	2.1±1.7
5	**26**	0.7±0.4	5.7±2.7	1.3±0.3	7.2±0.7	-	0.3±0.1	2.9±2.3
6	**33**	0.9±0.7	5.3±3.0	2.1±0.4	7.5±0.9	1.2±0.7	0.6±0.3	2.5±1.9

Notes: "-" means that no significant segregation or depletion is detected; the interfacial excess values of C, Cr, Mn and Mo were not measured (n.m.) and given for profile 1 since it is quite close to the GB carbide.

In order to explain this, the diffusion coefficients at low temperature (350°C) were estimated from the literature. After post welding heat treatment, the controlled cooling rate (15°C/s) is rather slow, while the subsequent air cooling (from 350°C to ambient temperature) is faster. Thus, we process on diffusion at 350°C. The mean diffusion distance at a GB is given by: $L = \sqrt{2D't}$, where D' is the diffusion coefficient along the GB and t is the corresponding time. The temperature dependence of diffusion kinetics is expressed by the equation: $D' = D_0 \exp(-\frac{Q_{GB}}{RT})$ [35], where D_0, Q_{GB}, T and R represent the pre-exponential factor, the activation energy for GB diffusion, the absolute temperature (523 K) and the gas constant (8.314 J/mol·K), respectively. Q_{GB} is roughly estimated to be about 50% of the activation energy for solute diffusion in bulk, Q [35]. According to the values of pre-exponential factor and activation energy (listed in Table 8 from the literature [36, 40-44]), the diffusion distances of P, Mn, Cr and Mo along the GBs at 350°C for 1 h were calculated and the results are shown in Table 8. Here, the C diffusion behavior was not calculated. This is because, during air cooling, C can interstitially diffuse and stabilize at a lower temperature than 350°C. For example, by adopting a D_o value of 0.02 cm^2/s and a Q value of 200 kJ/mol

348 [35], the diffusion distance of C in bulk crystal of α-iron is calculated to be 8.8 μm at 350°C
349 for 20 s and 9.3 μm at 250°C for 0.5 h. The theoretical diffusion distances of P, Mn, Cr and
350 Mo are large enough to allow solute redistribution along the GB. Thus, the evolution of
351 carbide does not modify the segregation behavior of the adjacent GB.

352 **Table 8 Calculation of diffusion distances (at 350°C for 1 h) for some chemical species along the GB**
353 **in the reference weld**

	D_o (cm²/s)	Q (kJ/mol)	D' (×10⁻¹⁰ cm²/s)	L (μm)
P [44]	0.25	200	10.3	27
Mn [42]	3.6	251.2	1.1	9
Cr [40]	37.3	267.4	2.3	13
Mo [36]	148	282.6	2.1	12

354 ## 4.2 Higher P segregation at the intersection between carbide and the adjacent GB

355 As shown in Table 7, there is a higher P segregation level at the intersection between
356 carbide and the adjacent HAGB.

357 This behavior was also observed for the intersection between cementite and a LAGB. Fig. 6
358 shows a cementite particle at a LAGB 12°[104]$(33\bar{2})/(\bar{1}\bar{3}1)$.

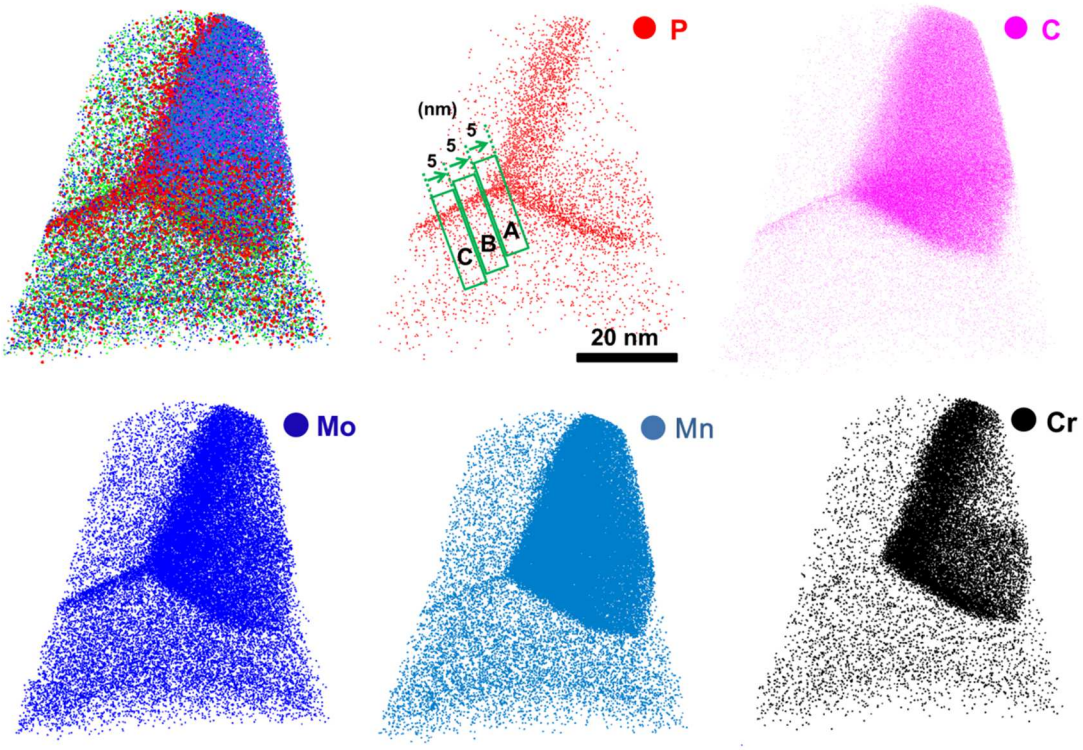

Fig. 6 Reconstructed P, C, Mo, Mn and Cr atom maps from a tip of the ion-irradiated weld. A large-sized cementite particle located on a LAGB 12°[104](33$\bar{2}$)/($\bar{1}\bar{3}$1) is visible, and the 3 green rectangles (marked as A, B and C) with a size of 5×20×20 nm^3 illustrate the locations where different concentration profiles were plotted for interfacial excess quantification.

By plotting concentration profiles through the LAGB 12°[104](33$\bar{2}$)/($\bar{1}\bar{3}$1) at different distances away from the cementite carbide, the variations of Gibbsian interfacial excess values were quantified. The results are reported in Table 9. Within the studied range of 5-15 nm away from the cementite carbide, there is no significant change in the segregation level of carbide forming elements like C, Cr, Mo and Mn. In contrast, the interfacial excess values of P from cuboids A, B and C are equal to be 3.4±1.9, 1.5±0.7, and 1.3±0.6 atoms/nm^2, respectively. This reveals that the P segregation level is higher at the intersection region between the carbide and the adjacent GB.

Table 9 Gibbsian interfacial excess values (in atoms/nm^2) in the LAGB shown on Fig. 6 at different

distances from the carbide.

Position	Distance from carbide (nm)	P	C	Si	Mn	Ni	Cr	Mo
A	**0**	3.4±1.9	n.m.	0.6±0.2	n.m.	4.4±2.8	n.m.	n.m.
B	**5**	1.5±0.7	5.4±1.7	0.7±0.2	4.1±0.5	2.4±1.5	0.3±0.2	2.2±1.6
C	**10**	1.3±0.6	4.6±1.2	0.05±0.01	3.9±0.4	2.9±1.6	0.4±0.2	3.0±1.7

Notes: the interfacial excess values of C, Cr, Mn and Mo were not measured (n.m.) and given for profile A since it is quite close to the GB carbide.

The solute segregation level at the interface boundary depends on the Gibbs free energy and the excess volume. As schematically illustrated in Fig. 7, three different regions can be distinguished for P segregation: the carbide-ferrite interface (region 1), the GB itself (region 2) and the intersection region (from the GB region to the carbide, region 3). The P segregation at regions 2 and 3 is much higher than that in region 1 (Fig. 7). For the general HAGB region (region 2), lots of free sites are available for solute segregation. As a result, the segregation level is high. The region 3 consists in the intersection between the carbide and the GB. In this region, the atomic arrangement is likely more disordered, which favors a higher P segregation than any other region. This agrees with the results reported in Table 7 & 9. It seems that the variation of the lattice misfit may be applied to explain the segregation change for the plate-like carbides along the GB (for example the cases in Fig. 7 with the carbide being stretched along the GB). The lattice misfit can be expressed by $\delta = (a_\beta - a_\alpha)/a_\alpha$, in which a_β and a_α represent the lattice parameters of adjacent phases separated by an interface [35]. If the misfit changes from one interface to another, a_β and a_α are met lattice parameters (which are constant) between the two phases. The maximum misfit is achieved perpendicular to the plate, namely, in region 3. In contrast, the atomic structure is more regular (as ferrite matrix) and the free energy is reduced in region 1. As a result, a lower segregation was observed in region 1.

393 The higher P segregation in region 3 was also observed for the intersection between cementite
394 and a LAGB. And this critical region (region 3) should be limited to several nanometers (less
395 than 5 nm as studied in this research).

396 For all carbides, interfaces with ferrite matrix can provide effective sites for P segregation.
397 The results reported in Table 5 exhibit a significant P segregation at the carbide-ferrite
398 interfaces. P atoms can diffuse from the ferrite matrix and segregate at the interface, and they
399 are also rejected from the carbide interior [15]. It is reported that the P solubility in carbide is
400 very low (close to 0) [14]. As the carbides grow, they continuously exclude the non-carbide
401 forming elements (P, Si and Ni) to interfaces and the surroundings. As shown in Table 3 & 4,
402 the P concentration is already nearly 0 inside the detected carbides.

403 According to our results, the P segregation level varies from one interface to another, and
404 its average value at cementite-ferrite interfaces is higher than that at $M_{2.0\text{-}3.2}C$ carbide-ferrite
405 interfaces for both reference and ion-irradiated welds. The segregation level at an interface is
406 correlated with the lattice coherency between the carbide and the ferrite, as well as the
407 corresponding Gibbs free energy. The segregation level varies in the range 0.03~0.8
408 atoms/nm^2 for the reference weld, while that appears in the range 0.11~2.9 atoms/nm^2 for the
409 ion-irradiated weld. Such large data scattering probably originates from structural variation of
410 these carbide-matrix interfaces [16]. The above-mentioned region 3 was also reported to be a
411 preferential nucleation site by creating Si-rich and P-rich environments [14].

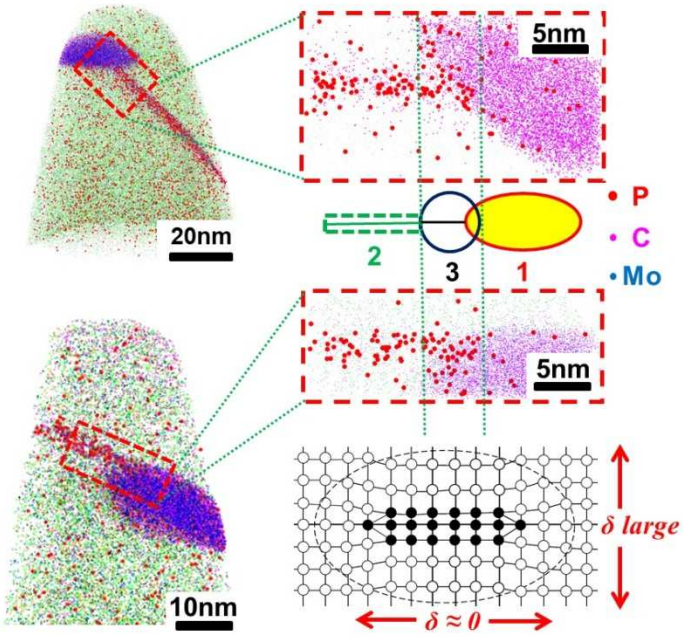

412

413 **Fig. 7 Schematic illustrations of P segregation behavior at boundaries or interfaces with the**
414 **reconstructed APT maps. Regions "1", "2" and "3" represent the carbide-ferrite interface, the GB**
415 **region and the intersection region from the GB region to the carbide-matrix interface, respectively; *δ***
416 **represents the lattice parameters of the two phases separated by an interface and the maximum**
417 **misfit is achieved perpendicular to the plate. The schematic illustration could be adapted to the**
418 **segregation behavior of other impurity elements.**

419 As discussed above, though the $M_{2.0\text{-}3.2}C$ carbides show no obvious influence on
420 segregation behavior at adjacent GBs (away from 5 nm to 36 nm), these carbides introduce
421 new potential sites for element segregation (P, Mn, Si and Ni). Indeed, the intersection region
422 (region 3) between a carbide and the GB region favors element segregation, in particular, a
423 higher P segregation than in other regions. Besides, the $M_{2.0\text{-}3.2}C$ carbide-ferrite interfaces also
424 enable element segregation (P, Mn, Si and Ni) but in a less content. Concerning cementite
425 carbides, their interfaces with ferrite matrix provide effective segregation sites for P, Si and
426 Ni. Similar to intergranular hydrogen embrittlement [45-47], the potential decohesion
427 resulting from the impurity segregation (as well as the local strain incompatibility) at these
428 carbide-ferrite interfaces may initiate or assist fracture process during plastic deformation.

High P segregation weakens chemical bonding of alloying elements at the interface, making it prone to cracking. This mechanism has been evidenced by observations of massive carbides on the fractured surfaces [11, 16].

4.3 Ion irradiation effects on P segregation at the carbide-ferrite interface

Ion irradiation leads to a clear increase of P segregation, with the Gibbsian interfacial excess values ranging from (0.4±0.2) to (1.4±0.5) atoms/nm^2 for cementite-ferrite interface and from (0.15±0.07) to (0.8±0.6) atoms/nm^2 for $M_{2.0\text{-}3.2}C$ carbide-ferrite interface, respectively. The supersaturation of Point Defects (PDs) was produced under ion irradiation, and thus RES or Radiation Induced Segregation (RIS) mechanism could be responsible for the solute segregation behavior [48]. In the former case, the solute mobility is enhanced by the supersaturation of mobile PDs (self-interstitials and vacancies), driven by the same thermodynamic force as under thermal ageing. The only impact of irradiation is to accelerate the evolution of the system towards its equilibrium state. In the latter case, not only the supersaturation of PDs is involved, but also fluxes of PDs moving towards the defect sinks such as free surfaces, GBs, dislocations and voids under irradiation. The coupling between the mobile PD fluxes and the solute fluxes will generate the solute segregation at PD sinks.

The irradiation mechanism is determined by the experimental parameters. Considering a dose rate of 1.3×10^{-5} dpa/s, an irradiation temperature (T) of 400°C and the melting point (T_m) at 1538°C (for pure iron), the T/T_m ratio is about 0.26. According to the coupling effect of temperature and dose rate from the literature [48], the current irradiation condition seems to correspond to the "recombination" domain (with a T/T_m ratio of 0.2-0.3). In multicomponent system, the diffusion kinetics is retarded and thus a significant RIS phenomenon may require higher temperature. In this case, the RES mechanism could be responsible for the increased P segregation. Under ion irradiation, the P segregation kinetics is enhanced because of the

presence of PD supersaturations. Since these PDs lead to high mutual recombination more than annihilation at PD sinks, the flux of PDs is quite low and the RIS mechanism may be not favored. This point was confirmed by our later research (to be published soon), based on the fact that P segregation at GBs reaches the same level as that under equilibrium thermal ageing at 400°C for 80000 h, and that other substitutional elements (Si+Mn+Cr+Mo+Ni) remain at the same segregation level as the unirradiated condition [49]. The influence of neutron irradiation with different fast neutron fluxes on the GB accumulation of P and the corresponding irradiation embrittlement tendency was studied in the VVER-1000 RPV welds, in which an accelerated neutron irradiation leads to a lower tendency to GB embrittlement compared with the irradiated samples with a much lower flux [9]. The flux effect should also be taken into account for the radiation enhanced P accumulation of practical RPV steels and welds.

In both reference and ion-irradiated welds, no solute depletion was observed. The RES of P under ion irradiation could contribute to the radiation embrittlement of the 16MND5 weld.

5. Conclusion

For the present research, the GB chemistry as well as the solute segregation behavior at carbide-ferrite interfaces was extensively quantified in both a reference weld and an ion-irradiated weld using APT technique. General conclusions can be made as follows:

1) The microstructure of the 16MND5 weld is mainly composed of acicular ferrite and intergranular carbides. There are two types of carbides in both reference and ion-irradiated welds: large cementite carbides and small $M_{2.0\text{-}3.2}C$ carbides. The Fe concentration is larger than 50 at.% in cementite, and the outer layers of these carbides are not chemically homogeneous (with a clear Mo, Mn and Cr enrichment). In the detected $M_{2.0\text{-}3.2}C$ carbides, Mo shares over 35 at.% and the Fe concentration is less than 30 at.%.

2) The intergranular carbides show no influence on element segregation behavior of the

vicinal GBs (within the investigated distance 5-36 nm). However, these carbides introduce effective sites for solute segregation (P, Mn, Si and Ni). The co-segregation of one or several chemical species (Ni, Si and P) was observed for the detected interfaces. Particularly, there is an obvious Mn segregation at $M_{2.0\text{-}3.2}C$ carbide-ferrite interfaces. The intersection region between carbide and the adjacent GB also favors element segregation, in particular, a higher P segregation than in any other region. The potential decohesion resulting from the impurity segregation at carbide-matrix interfaces or the intersection regions may initiate or assist fracture process during plastic deformation.

3) Ion irradiation, in the present conditions, does not change the carbide. However, under ion irradiation, P segregation at carbide-ferrite interfaces increases. The increased P segregation at both types of carbides could be due to a RES mechanism, leading to an irradiation embrittlement of the 16MND5 welds. The average P segregation level is higher in cementite-ferrite interfaces than $M_{2.0\text{-}3.2}C$ carbide-ferrite interfaces under both conditions.

Acknowledgement

This work was performed on the GENESIS platform, financially supported by Centre National de la Recherche Scientifique (CNRS) belonging to the project entitled “Investissements d’avenir” with a reference number ANR-11-EQPX-0020. This work is part of the EM2VM Joint Laboratory Study and Modeling of the Microstructure for Ageing of Materials. This work was supported by the MAI-sn (Materials Ageing Institute-Scientific Network, http://themai.org/scientific-network).

The authors also owe their sincere gratitude to Prof. Didier Blavette for the fruitful discussions.

Research Data

Data not available / Data will be made available on request.

References:

[1] G. Kuri, S. Cammelli, C. Degueldre, J. Bertsch, D. Gavillet, Neutron induced damage in reactor pressure vessel steel: An X-ray absorption fine structure study, J Nucl Mater, 385(2009) 312-318.

[2] M.K. Miller, K.F. Russell, J. Kocik, E. Keilova, Embrittlement of low copper VVER 440 surveillance samples neutron-irradiated to high fluences, J Nucl Mater, 282(2000) 83-88.

[3] M.K. Miller, K.F. Russell, M.A. Sokolov, R.K. Nanstad, APT characterization of irradiated high nickel RPV steels, J Nucl Mater, 361(2007) 248-261.

[4] M.K. Miller, K.F. Russell, M.A. Sokolov, R.K. Nanstad, Atom probe tomography characterization of radiation-sensitive KS-01 weld, J Nucl Mater, 320(2003) 177-183.

[5] B.A. Gurovich, E.A. Kuleshova, Y.I. Shtrombakh, D.Y. Erak, A.A. Chernobaeva, O.O. Zabusov, Fine structure behaviour of VVER-1000 RPV materials under irradiation, J Nucl Mater, 389(2009) 490-496.

[6] B.A. Gurovich, E.A. Kuleshova, Y.A. Nikolaev, Y.I. Shtrombakh, Assessment of relative contributions from different mechanisms to radiation embrittlement of reactor pressure vessel steels, J Nucl Mater, 246(1997) 91-120.

[7] B.A. Gurovich, E.A. Kuleshova, Y.I. Shtrombakh, O.O. Zabusov, E.A. Krasikov, Intergranular and intragranular phosphorus segregation in Russian pressure vessel steels due to neutron irradiation, J Nucl Mater, 279(2000) 259-272.

[8] E.A. Kuleshova, B.A. Gurovich, Z.V. Lavrukhina, M.A. Saltykov, S.V. Fedotova, A.N. Khodan, Assessment of segregation kinetics in water-moderated reactors pressure vessel steels under long-term operation, J Nucl Mater, 477(2016) 110-122.

[9] E.A. Kuleshova, B.A. Gurovich, Z.V. Lavrukhina, D.A. Maltsev, S.V. Fedotova, A.S. Frolov, G.M. Zhuchkov, Study of the flux effect nature for VVER-1000 RPV welds with high nickel content, J Nucl Mater, 483(2017) 1-12.

[10] M.K. Miller, M.G. Burke, An atom probe field ion microscopy study of neutron-irradiated pressure vessel steels, J Nucl Mater, 195(1992) 68-82.

[11] B. Gurovich, E. Kuleshova, O. Zabusov, S. Fedotova, A. Frolov, M. Saltykov, D. Maltsev, Influence of structural parameters on the tendency of VVER-1000 reactor pressure vessel steel to temper embrittlement, J Nucl Mater, 435(2013) 25-31.

[12] L. Lundin, B. Richarz, Atom-probe study of phosphorus segregation to the carbide/matrix interface in an aged 9% chromium steel, Appl Surf Sci, 87(1995) 194-199.

[13] R. Moller, S.S. Brenner, A.J. Grabke, The effect of molybdenum on the grain boundary segregation of

phosphorus in steel, Scripta Metall Mater, 20(1986) 587-592.

[14] M.I. Isik, A. Kostka, V.A. Yardley, K.G. Pradeep, M.J. Duarte, P. Choi, D. Raabe, G. Eggeler, The nucleation of Mo-rich Laves phase particles adjacent to M23C6 micrograin boundary carbides in 12% Cr tempered martensite ferritic steels, Acta Mater, 90(2015) 94-104.

[15] C. Philippot, K. Hoummada, M. Dumont, J. Drillet, V. Hebert, P. Maugis, Influence of a 2-D defect on the partitioning during the formation of a cementite particle in steels, Comp Mater Sci, 106(2015) 64-68.

[16] J. Dong, M. Zhang, X. Xie, R.G. Thompson, Interfacial segregation and cosegregation behaviour in a nickel-base alloy 718, Mater Sci Eng A - Struct, 328(2002) 8-13.

[17] Y.F. Jiang, B. Zhang, Y. Zhou, J.Q. Wang, E. Han, W. Ke, Atom probe tomographic observation of hydrogen trapping at carbides/ferrite interfaces for a high strength steel, J Mater Sci Technol, 34(2018) 1344-1348.

[18] M.K. Miller, R.G. Forbes, Atom-probe tomography: the local electrode atom probe, Springer Science & Business Media, New York, 2014.

[19] M. Herbig, Spatially correlated electron microscopy and atom probe tomography: Current possibilities and future perspectives, Scripta Mater, 148(2018) 98-105.

[20] M. Herbig, D. Raabe, Y.J. Li, P. Choi, S. Zaefferer, S. Goto, Atomic-scale quantification of grain boundary segregation in nanocrystalline material, Phys Rev Lett, 112(2014) 126103.

[21] D. Raabe, M. Herbig, S. Sandlöbes, Y. Li, D. Tytko, M. Kuzmina, D. Ponge, P. Choi, Grain boundary segregation engineering in metallic alloys: A pathway to the design of interfaces, Curr Opin Solid St M, 18(2014) 253-261.

[22] V. Randle, Application of EBSD to the analysis of interface planes: evolution over the last two decades, J Microsc, 230(2008) 406-413.

[23] A.D. Rollett, S. Lee, R. Campman, G.S. Rohrer, Three-dimensional characterization of microstructure by electron back-scatter diffraction, Annu Rev Mater Res, 37(2007) 627-658.

[24] K. Babinsky, W. Knabl, A. Lorich, R. De Kloe, H. Clemens, S. Primig, Grain boundary study of technically pure molybdenum by combining APT and TKD, Ultramicroscopy, 159(2015) 445-451.

[25] S. Mandal, K.G. Pradeep, S. Zaefferer, D. Raabe, A novel approach to measure grain boundary segregation in bulk polycrystalline materials in dependence of the boundaries' five rotational degrees of freedom, Scripta Mater, 81(2014) 16-19.

[26] K. Babinsky, R. De Kloe, H. Clemens, S. Primig, A novel approach for site-specific atom probe

562 specimen preparation by focused ion beam and transmission electron backscatter diffraction,
563 Ultramicroscopy, 144(2014) 9-18.
564 [27] L. Yao, S.P. Ringer, J.M. Cairney, M.K. Miller, The anatomy of grain boundaries: Their structure and
565 atomic-level solute distribution, Scripta Mater, 69(2013) 622-625.
566 [28] L. Zhang, B. Radiguet, P. Todeschini, C. Domain, Y. Shen, P. Pareige, Investigation of solute
567 segregation behavior using a correlative EBSD/TKD/APT methodology in a 16MND5 weld, J Nucl
568 Mater, 523(2019) 434-443.
569 [29] A. Akhatova, F. Christien, V. Barnier, B. Radiguet, E. Cadel, F. Cuvilly, P. Pareige, Investigation of the
570 dependence of phosphorus segregation on grain boundary structure in Fe-P-C alloy: cross comparison
571 between Atom Probe Tomography and Auger Electron Spectroscopy, Appl Surf Sci, 463(2019) 203-210.
572 [30] A.S. ASTM, Standard Practice for Neutron Radiation Damage Simulation by Charged-Particle
573 Irradiation, ASTM International, West Conshohocken, PA (2009) E521-96.
574 [31] M. Thuvander, J. Weidow, J. Angseryd, L.K. Falk, F. Liu, M. Sonestedt, K. Stiller, H. Andrén,
575 Quantitative atom probe analysis of carbides, Ultramicroscopy, 111(2011) 604-608.
576 [32] B.W. Krakauer, D.N. Seidman, Absolute atomic-scale measurements of the Gibbsian interfacial excess
577 of solute at internal interfaces, Phys Rev B, 48(1993) 6724.
578 [33] R.A. Farrar, P.L. Harrison, Acicular ferrite in carbon-manganese weld metals: an overview, J Mater Sci,
579 22(1987) 3812-3820.
580 [34] P. Auger, P. Pareige, S. Welzel, J.C. Van Duysen, Synthesis of atom probe experiments on irradiation-
581 induced solute segregation in French ferritic pressure vessel steels, J Nucl Mater, 280(2000) 331-344.
582 [35] D.A. Porter, K.E. Easterling, M. Sherif. Phase Transformations in Metals and Alloys, (Revised Reprint),
583 CRC press, 2009.
584 [36] H. Nitta, T. Yamamoto, R. Kanno, K. Takasawa, T. Iida, Y. Yamazaki, S. Ogu, Y. Iijima, Diffusion of
585 molybdenum in α-iron, Acta Mater, 50(2002) 4117-4125.
586 [37] P. Pareige, P. Auger, J. Van Duysen, Effets de l'irradiation aux neutrons sur le vieillissement de l'acier
587 de la cuve de réacteurs électronucléaires: observation à l'échelle de l'atome par sonde atomique, Le
588 Journal de Physique IV, 11(2001) 1-39.
589 [38] D. Raabe, S. Sandlöbes, J. Millán, D. Ponge, H. Assadi, M. Herbig, P. Choi, Segregation engineering
590 enables nanoscale martensite to austenite phase transformation at grain boundaries: a pathway to ductile
591 martensite, Acta Mater, 61(2013) 6132-6152.

[39] Y.J. Li, P. Choi, S. Goto, C. Borchers, D. Raabe, R. Kirchheim, Evolution of strength and microstructure during annealing of heavily cold-drawn 6.3 GPa hypereutectoid pearlitic steel wire, Acta Mater, 60(2012) 4005-4016.

[40] C. Lee, Y. Iijima, T. Hiratani, K. Hirano, Diffusion of chromium in α-iron, Mater Trans, JIM, 31(1990) 255-261.

[41] G. Luckman, R.A. Didio, W.R. Graham, Phosphorus interdiffusivity inα-Fe binary and alloy systems, Metall Trans A, 12(1981) 253-259.

[42] V. Irmer, M. Feller-Kniepmeier, Diffusion of manganese in α-iron single crystals of different purity, J Phys Chem Solids, 33(1972) 2141-2148.

[43] G. Siebel, Comptes Rendus, Mem Sci Rev Metall, 61(1964) 413-434.

[44] S.G. Druce, G. Gage, G. Jordan, Effect of ageing on properties of pressure vessel steels, Acta Metall Mater, 34(1986) 641-652.

[45] P. Novak, R. Yuan, B.P. Somerday, P. Sofronis, R.O. Ritchie, A statistical, physical-based, micro-mechanical model of hydrogen-induced intergranular fracture in steel, J Mech Phys Solids, 58(2010) 206-226.

[46] J. Kameda, C.J. McMahon, Solute segregation and brittle fracture in an alloy steel, Metall Mater Trans A, 11(1980) 91-101.

[47] J. Kameda, C.J. McMahon, Solute segregation and hydrogen-induced intergranular fracture in an alloy steel, Metall Trans A, 14(1983) 903-911.

[48] M. Nastar, F. Soisson, 1.18 Radiation induced segregation. Comprehensive nuclear materials, Elsevier, 1(2012) 471-496.

[49] L. Zhang, B. Radiguet, P. Todeschini, C. Domain, Y. Shen, P. Pareige, Thermal-Ageing and Ion-Irradiation Enhanced Intergranular P Segregation in Low Alloy Steel Welds. Available at SSRN: https://ssrn.com/abstract=3659823 or http://dx.doi.org/10.2139/ssrn.3659823.

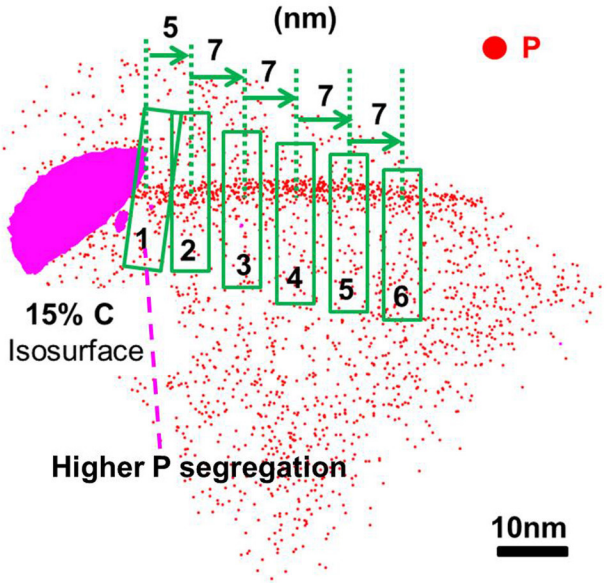
(nm)
5
7
7
7
7
P
1
2
3
4
5
6
15% C
Isosurface
Higher P segregation
10nm

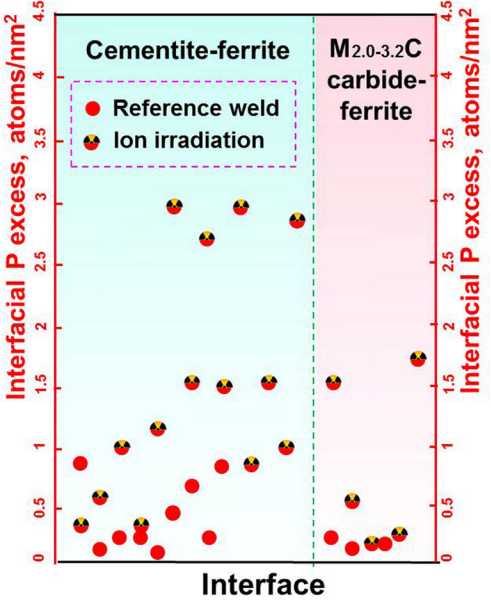
Cementite-ferrite
M2.0-3.2C carbide-ferrite
Reference weld
Ion irradiation
Interfacial P excess, atoms/nm2
Interfacial P excess, atoms/nm2
0
0.5
1
1.5
2
2.5
3
3.5
4
4.5
Interface